Ferromagnetism by *p-d* exchange spin-orbit coupling in *n*-type ferromagnetic semiconductors

Kenji Hayashida*

Division of Applied Physics, Graduate School of Engineering, Hokkaido University, Sapporo, Hokkaido 060-8628, Japan

(Received 16 December 2022; revised 19 February 2023; accepted 14 April 2023; published 26 April 2023)

The exchange interaction between carrier and localized spin in magnets generates intrinsic spin-orbit coupling induced by the magnetism. Recent studies for the exchange spin-orbit coupling (ESOC) in ferromagnets and antiferromagnets suggest the ESOC and the transport phenomena for spintronics. However, the study on the effects of ESOC on the magnetic phase transition has been still lacking especially for ferromagnets even though the ESOC should be one of the fundamental interactions to stabilize the magnetic phase. In this paper, we study the role of the ferromagnetic properties of the ESOC induced by the *p-d* exchange interaction of the valence band in *n*-type ferromagnetic semiconductors. Based on the mean-field and $\boldsymbol{k}\cdot\boldsymbol{p}$ methods, our theory explains the spin polarization of localized and carrier spin, and the Curie temperature T_c for the iron concentration, electron density, and host semiconductor dependence. The theoretical T_c fits experimental values well in low iron concentration and intermediate electron density regions, and the *p-d* exchange interaction is essential for T_c. Furthermore, the T_c is higher for narrower gap host semiconductors to provide insights into higher T_c. The theoretical framework of this paper is not limited to the specific materials and will find potential materials for spintronics and the fundamental aspects.

DOI: 10.1103/PhysRevB.107.165203

I. INTRODUCTION

Exchange spin-orbit coupling (ESOC) is an effect of the exchange interaction between carrier and magnetic order in an electronic structure and has attracted much attention for the mechanisms and spintronics applications [1–11]. In energy bands, ESOC generates $\boldsymbol{k}$ (wave-vector)-dependent spin splitting induced by the exchange interaction of carrier spin with antiferromagnetic [1,2,4–10,12–14] or ferromagnetic [11] order. Recent theories [1,4,5,7–10] and experiments [2,3,15] for the ESOC in antiferromagnets suggested the electronic structure and spin Hall-like effect for spin torque generation. In our previous paper, we have shown that the ESOC is generated in the conduction band (CB) of *n*-type ferromagnetic semiconductors (*n*-type FMSs) by the *p-d* exchange interaction of the valence band [11] through the interband transition in the same manner as the relativistic spin-orbit coupling is produced by the LS coupling and that the *p-d* ESOC shows a remarkable anomalous Hall effect of the intrinsic origin as an effect on transport properties. Note that the study on RuO_2 uses the term, altermagnetism, for magnetically induced $\boldsymbol{k}$-dependent band structure rather than the term utilized in this paper, ESOC [6]. Both concepts have been developing and currently differ in their theoretical foundations and magnetic structure. Altermagnetism requires a specific group consistent with crystal symmetry and antiferromagnetic structure. ESOC is based on interband transition and exchange interaction in ferromagnets [11]. However, the two terms share magnetism-induced spin-orbit coupling and nonrelativistic origin as the fundamental feature.

However, the role of ESOC in ferromagnetic properties has not been studied even though the ESOC coexists with magnetic order and should be one of the fundamental interactions to stabilize the magnetic phase. Especially, the ESOC effects on the magnetic phase transition in ferromagnets have been still lacking. The tunneling spectroscopy observing spin splitting of the conduction band [16] estimated the Curie temperature T_c of an iron-doped InAs (InFeAs, *n*-type FMS) [16–18] from the mean-field theory [19,20] and without the *p-d* ESOC. The estimated values were several kelvins and did not match experimental values, 42 and 65 kelvin for Fe 6 and 8% samples, which the tunneling spectroscopy [16] simultaneously measured. The *p-d* exchange interaction in the valence band, which is larger than the *s-d* exchange interaction in the conduction band, is expected to account for large experimental T_c values since the *p-d* exchange interaction emerges in the conduction band through the $\boldsymbol{k}\cdot\boldsymbol{p}$ interband transition.

n-type FMSs (InFeAs [16–18] and InFeSb [21–23]) are iron-doped ferromagnetic III–V semiconductors [24] showing ferromagnetism and have been studied for spintronics applications, such as the manganese-doped III–V semiconductors [19,20,25–30]. The iron impurity works only as a magnetic impurity and other impurities introduce carriers. For example, the beryllium atom works as a double donor in InFeAs [16–18]. Interestingly, the T_c of the narrower gap host semiconductor (InFeSb) [21–23] is higher than the large gap host semiconductor (InFeAs) [24].

In this paper, we study the ferromagnetic properties (T_c and spin polarization of localized and carrier spin) of *n*-type FMSs by the *p-d* exchange interaction and interband transition. We construct a mean-field theory with the $\boldsymbol{k}\cdot\boldsymbol{p}$ method to investigate the dependences of the Curie temperature T_c on the iron concentration, electron density, and host semiconductor.

*globalpenguin811@gmail.com

First, the mean-field theory fits the experimental T_c well for the low iron concentration region. The calculated T_c increases linearly with the iron concentration, whose behavior is one of the characteristics of the mean-field approximation [19,20,30]. We also confirm that the T_c without the p-d exchange interaction is lower than 1 kelvin, and this small T_c is consistent with the tunneling spectroscopy estimation [16]. The p-d exchange interaction with the interband transition (p-d ESOC) is essential for T_c of n-type FMSs.

Second, we investigate the electron-density dependence of T_c for InFeAs (Fe 5%). The T_c is independent of the electron density, and this indicates that the ferromagnetism by p-d ESOC does not require the Fermi surface.

The theoretical T_c for the electron-density dependence fits the experimental one in the same order for the intermediate density region. However, the experiment has revealed that the T_c rises sharply at the critical electron density of 0.6×10^{19} cm^{-3} [24]. This drastic increase in T_c indicates the transition for Anderson localization by disorder [31] and Mott transition by electron correlation [32] through carrier doping. The localization transition is typical in doped semiconductors [33] and has been discussed also for the manganese-doped p-type FMSs [28,30]. This transition sets the lower bound for the comparison of the theoretical T_c with the experimental one in the electron-density dependence since our theory neglects the impurity potential and electron correlation for the electronic state. We also consider only the conduction band at the Γ point in the first Brillouin zone, but other conduction bands appear for the relatively high-electron doping to induce the upper bound of the comparable region. We obtain the T_c, which is on the same order as experimental T_c in the comparable region and attribute the deviation between the theoretical and the experimental T_c's outside the region to the localization effects and higher-conduction bands.

Furthermore, for InFeAs, we investigate the chemical potential μ dependence of T_c to understand the behavior of the considered $\boldsymbol{k} \cdot \boldsymbol{p}$ model for T_c and show that the model depending on μ becomes the virtually p-type FMS, bulk band insulator ferromagnet and n-type FMS.

Finally, we study the T_c of InFeSb to get insights into the host semiconductor dependence. The mean-field theory shows the higher T_c of the narrower gap host semiconductor, and this host semiconductor dependence is consistent with experiments [24]. We explain this dependence from the p-d ESOC of the conduction band [11] qualitatively. The perturbative effective Hamiltonian for the ESOC [11] is proportional to the E_g^{-1} in the lowest order in which E_g is the fundamental energy gap of the host semiconductor and is assumed to be the largest energy scale. Therefore, the narrower energy gap provides larger p-d ESOC and leads to higher T_c.

This paper investigated n-type FMSs. However, the theoretical framework combining the $\boldsymbol{k} \cdot \boldsymbol{p}$ method with the mean-field approximation is applicable to other materials, for example, itinerant antiferromagnet RuO_2 [1–4,6,12–15] and a doped organic antiferromagnet [34]. One of the interesting materials for the application of the framework is an FMS quantum well (InFeAs/GaFeSb) since both InFeAs and GaFeSb [35,36] have been already fabricated, and we can expect a quantum anomalous Hall effect [37]. The manganese-type quantum well (InMnAs/GaMnSb) is predicted to show the quantum anomalous Hall effect [38], but the experimental realization is hard since the manganese ion works as an acceptor as well as magnetic impurity [39]. The iron impurity works just as a magnetic ion and we can independently tune carrier density in InFeAs/GaFeSb to avoid the problem of InMnAs/GaMnSb. We can investigate the role of the ESOC for the quantum anomalous Hall effect in InFeAs/GaFeSb with higher feasibility. Application of the framework to other materials as the iron-type FMS quantum well will uncover further ESOCs and central roles in magnetism and transport phenomena.

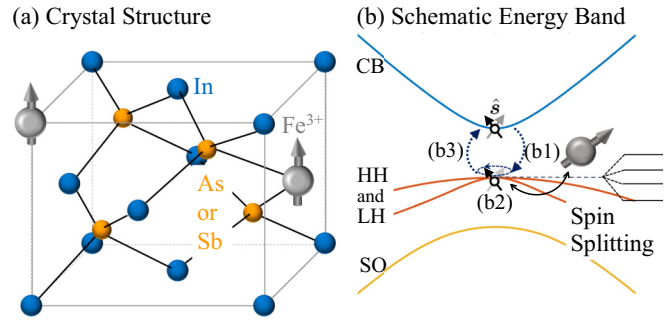

FIG. 1. (a) Crystal structure of n-type FMSs. The fundamental structure is the zinc-blende structure. The iron ion spins (Fe^{3+} spins) randomly occupy the indium sites and donors introduce conduction electrons. (b) Schematic energy bands of n-type FMSs and mechanism of spin-orbit coupling in the CB. We depict the spin splitting originating from the p-d exchange interaction between carrier spin $\hat{\boldsymbol{s}}$ and Fe^{3+} spins in heavyhole (HH) and lighthole (LH) bands (we omit the spin splitting in CB and SO bands for brevity). Spin-orbit coupling of CB appears as $\boldsymbol{k}$ (wave-vector)-dependent spin rotation both for relativistic and exchange SOC. The $\boldsymbol{k} \cdot \boldsymbol{p}$ mechanism follows a procedure (b1)–(b3). At first, the electron in the CB moves to one of the valence bands by $\boldsymbol{k}$-dependent interband transition (b1). Second, the electron spin rotates by the spin-dependent interaction (exchange interaction is depicted in the figure) (b2). Finally, the rotating spin returns to the CB through the interband transition, and we observe the spin rotation of the CB electron (b3).

The structure of this paper is the follows. Section II A represents the crystal structure and the $\boldsymbol{k} \cdot \boldsymbol{p}$ method. Sections II B–II D explain the Hamiltonian and self-consistent equations. Finally, Sec. II E shows the energy bands and assumptions for our theory. Sections III A and III B describe the iron concentration and electron-density dependence of T_c in InFeAs. Section III C investigates the T_c of InFeSb to discuss the host semiconductor dependence. Section IV represents the conclusion of this paper.

II. METHOD

A. Crystal structure and the $\boldsymbol{k} \cdot \boldsymbol{p}$ method

The crystal structure of n-type FMSs, such as $In_{1-x}Fe_xAs$ and $In_{1-x}Fe_xSb$ is the zinc-blende structure with randomly distributed iron impurities at the indium atom sites by x percent [Fig. 1(a)]. The band structure is also the III–V semiconductor type with spin splitting by the exchange interactions between electrons and localized spins (d orbital) at each band. The conduction and valence bands host s-d and p-d exchange interactions at the band edges, respectively,

since the orbital characters of each band edge are *s* and *p* orbitals [Fig. 1(b)].

To investigate the band structure, we can take a $\boldsymbol{k}\cdot\boldsymbol{p}$ method to fully account for the multiple energy bands or an effective Hamiltonian method based on a perturbative way [11]. The effective Hamiltonian method cannot be applied to a narrower gap or broken gap FMS. We use the $\boldsymbol{k}\cdot\boldsymbol{p}$ and effective Hamiltonian methods for quantitative and qualitative understandings of T_c, respectively.

The $\boldsymbol{k}\cdot\boldsymbol{p}$ method incorporates the effects of the valence band on the conduction band at nonzero $\boldsymbol{k}$ points through the $\boldsymbol{k}\cdot\boldsymbol{p}$ interband transition, and one of the representative $\boldsymbol{k}\cdot\boldsymbol{p}$ effects is the effective mass of the conduction band [40]. The $\boldsymbol{k}\cdot\boldsymbol{p}$ method also explains relativistic (Rashba [41–44] and Dresselhaus [45]) and nonrelativistic (*p-d* exchange) [11] spin-orbit coupling. Figure 1(b) depicts the schematic for relativistic and exchange SOCs in a unified manner. The electron in the conduction band moves to one of the valence bands through the $\boldsymbol{k}\cdot\boldsymbol{p}$ interband transition, which is proportional to $\boldsymbol{k}$ [(b1) in Fig. 1(b)]. The electron spin rotates due to spin-dependent interaction, such as exchange interaction or relativistic spin-orbit coupling [(b2)]. After the electron returns to the conduction band, the spin interaction results in the effective rotation in the conduction band and the $\boldsymbol{k}$-dependent spin-orbit coupling [(b3)].

B. Total Hamiltonian

The total Hamiltonian is

$$H = H_0 + H_{\mathrm{ex,c}} + H_{\mathrm{ex,S}}, \tag{1}$$

in which H_0, $H_{\mathrm{ex,c}}$, and $H_{\mathrm{ex,S}}$ describe the $\boldsymbol{k}\cdot\boldsymbol{p}$ Hamiltonian of the host semiconductor, *s*, *p-d* exchange interactions of the carrier spin with the localized spin polarization,which is proportional to the magnetization of the FMS [11] and exchange interaction of the localized spins with the carrier spin polarization density, respectively. In the exchange interactions, we include only spacially uniform components of the *s*, *p-d* exchange interaction as the literature [46]. Furthermore, we employ the virtual crystal approximation and the mean-field approximation [19,20,30]. The band parameters used in this paper are summarized in Appendix B. We describe the specific forms of each term.

C. Hamiltonian of the host semiconductor

Using the quasidegenerate perturbation theory and basis functions (Table I) [47], we obtain the Hamiltonian of the host semiconductor,

$$H_0 = \begin{bmatrix} H_c & H_{cv} \\ H_{cv}^{\dagger} & H_v \end{bmatrix},$$

with the conduction H_c, valence H_v, and interband H_{cv} blocks. We use suggested values for the band parameters [47,48] and set *x*, *y*, and *z* axes to [100], [010], and [001] directions of the host semiconductor, respectively.

The conduction-band block H_c is

$$H_c = \frac{\hbar^2 k^2}{2m_c'}\hat{1}_\sigma, \quad k = |\boldsymbol{k}|$$

TABLE I. Basis functions for the representation of the total Hamiltonian. $|S\rangle$ is an *s*-like orbital of the CB edge. $|X\rangle$, $|Y\rangle$, and $|Z\rangle$ represent *p*-like orbitals of the valence-band edges (HH, LH, and SO). $|\uparrow\rangle$ and $|\downarrow\rangle$ express up-spin and down-spin states. The quantization axis is the *z* axis. We set the phases of the *s*- and *p*-like orbitals as real and pure imaginary, respectively [47].

Band	Function
CB	$\lvert S,\uparrow\rangle$
CB	$\lvert S,\downarrow\rangle$
HH	$-\frac{1}{\sqrt{2}}(\lvert X,\uparrow\rangle + i\lvert Y,\uparrow\rangle)$
LH	$-\frac{1}{\sqrt{6}}(\lvert X,\downarrow\rangle + i\lvert Y,\downarrow\rangle) + \sqrt{\frac{2}{3}}\lvert Z,\uparrow\rangle$
LH	$\frac{1}{\sqrt{6}}(\lvert X,\uparrow\rangle - i\lvert Y,\uparrow\rangle) + \sqrt{\frac{2}{3}}\lvert Z,\downarrow\rangle$
HH	$\frac{1}{\sqrt{2}}(\lvert X,\downarrow\rangle - i\lvert Y,\downarrow\rangle)$
SO	$-\frac{1}{\sqrt{3}}(\lvert X,\downarrow\rangle + i\lvert Y,\downarrow\rangle) - \frac{1}{\sqrt{3}}\lvert Z,\uparrow\rangle$
SO	$-\frac{1}{\sqrt{3}}(\lvert X,\uparrow\rangle - i\lvert Y,\uparrow\rangle) + \frac{1}{\sqrt{3}}\lvert Z,\downarrow\rangle$

$$\frac{m_0}{m_c'} = \frac{m_0}{m_c} - \frac{E_P}{3}\left(\frac{2}{E_g} + \frac{1}{E_g+\Delta_g}\right),$$
$$E_P = \frac{2m_0}{\hbar^2}P^2, \tag{2}$$

in which $\boldsymbol{k}$ is a wave vector, $\hbar$ is a Planck constant divided by 2π, and m_0 is the electron mass in a vacuum. $\hat{1}_\sigma$ represents the 2×2 identity matrix, m_c is the effective mass at the conduction-band edge and determined from the experimental value [48]. E_g and Δ_g are the fundamental and split-off gaps, respectively. P is the Kane matrix [40].

The valence-band block H_v is

$$H_v = \begin{bmatrix} h_{v11} & h_{v12} & h_{v13} & 0 & h_{v15} & h_{v16} \\ & h_{v22} & 0 & h_{v13} & h_{v25} & h_{v26} \\ & & h_{v22} & -h_{v12} & h_{v26}^* & -h_{v25} \\ & \dagger & & h_{v11} & -h_{v16}^* & h_{v15}^* \\ & & & & h_{v55} & 0 \\ & & & & & h_{v55} \end{bmatrix}$$
$$- \mathrm{diag}[E_g, E_g, E_g, E_g, E_g+\Delta_g, E_g+\Delta_g]$$
$$+ C_k \begin{bmatrix} 0 & -\frac{1}{2}k_+ & k_z & -\frac{\sqrt{3}}{2}k_- & \frac{1}{2\sqrt{2}}k_+ & \frac{1}{\sqrt{2}}k_z \\ & 0 & \frac{\sqrt{3}}{2}k_+ & -k_z & 0 & -\frac{\sqrt{3}}{2\sqrt{2}}k_+ \\ & & 0 & -\frac{1}{2}k_+ & \frac{\sqrt{3}}{2\sqrt{2}}k_- & 0 \\ & & & 0 & \frac{1}{\sqrt{2}}k_z & -\frac{1}{2\sqrt{2}}k_- \\ & \dagger & & & 0 & 0 \\ & & & & & 0 \end{bmatrix},$$

in which $\mathrm{diag}[x, y, z, \ldots]$ represents the diagonal matrix containing $x, y, z, \ldots$ for the diagonal components. The specific components in the first term are

$$h_{v11} = -\frac{\hbar^2}{2m_0}(\gamma_1' + \gamma_2')\left(k_x^2 + k_y^2\right) - \frac{\hbar^2}{2m_0}(\gamma_1' - 2\gamma_2')k_z^2,$$
$$h_{v22} = -\frac{\hbar^2}{2m_0}(\gamma_1' - \gamma_2')\left(k_x^2 + k_y^2\right) - \frac{\hbar^2}{2m_0}(\gamma_1' + 2\gamma_2')k_z^2,$$
$$h_{v55} = -\frac{\hbar^2}{2m_0}\gamma_1' k^2,$$

$$h_{v12} = 2\sqrt{3}\frac{\hbar^2}{2m_0}\gamma_3' k_z k_-,$$
$$h_{v13} = \sqrt{3}\frac{\hbar^2}{2m_0}\gamma_2'\left(k_x^2 - k_y^2\right) - 2i\sqrt{3}\frac{\hbar^2}{2m_0}\gamma_3' k_x k_y,$$
$$h_{v15} = -\sqrt{6}\frac{\hbar^2}{2m_0}\gamma_3' k_z k_-,$$
$$h_{v16} = -\sqrt{6}\frac{\hbar^2}{2m_0}\gamma_2'\left(k_x^2 - k_y^2\right) + 2i\sqrt{6}\frac{\hbar^2}{2m_0}\gamma_3' k_x k_y,$$
$$h_{v25} = -\sqrt{2}\frac{\hbar^2}{2m_0}\gamma_2'\left(k_x^2 + k_y^2 - 2k_z^2\right),$$
$$h_{v26} = 3\sqrt{2}\frac{\hbar^2}{2m_0}\gamma_3' k_z k_-.$$

The reduced-band parameters γ_i' [47] to represent remote-band effects are

$$\gamma_1' = \gamma_1 - \frac{1}{3}\frac{E_P}{E_g},$$
$$\gamma_2' = \gamma_2 - \frac{1}{6}\frac{E_P}{E_g},$$
$$\gamma_3' = \gamma_3 - \frac{1}{6}\frac{E_P}{E_g},$$

in which γ_i is the Luttinger parameter [48,49]. For the C_k parameter, we use the value of the literature [47].

The interband block H_{cv} is

$$H_{cv} = \begin{bmatrix} h_{cv1} & h_{cv2} & \frac{1}{\sqrt{3}}h_{cv3} & 0 & \frac{-1}{\sqrt{2}}h_{cv2} & -\sqrt{\frac{2}{3}}h_{cv3} \\ 0 & \frac{1}{\sqrt{3}}h_{cv1} & h_{cv2} & h_{cv3} & \sqrt{\frac{2}{3}}h_{cv1} & \frac{1}{\sqrt{2}}h_{cv2} \end{bmatrix},$$

in which

$$h_{cv1} = -\frac{1}{\sqrt{2}}Pk_+ + \frac{1}{\sqrt{2}}B'k_z k_-,$$
$$h_{cv2} = \sqrt{\frac{2}{3}}Pk_z + i\sqrt{\frac{2}{3}}B'k_x k_y,$$
$$h_{cv3} = \frac{1}{\sqrt{2}}Pk_- + \frac{1}{\sqrt{2}}B'k_z k_+.$$

For the B' parameter, we use an average value of related parameters (B_{8v}^+ and B_{7v} in Ref. [47]).

D. Exchange interactions and self-consistent equation

The exchange interactions are

$$H_{\mathrm{ex,c}} = -\hat{P}_c\hat{\boldsymbol{s}}\cdot\boldsymbol{h}_{\mathrm{eff},c} - \hat{P}_v\hat{\boldsymbol{s}}\cdot h_{\mathrm{eff},v},$$
$$H_{\mathrm{ex,S}} = -\sum_I \boldsymbol{H}_{\mathrm{eff}}\cdot\hat{\boldsymbol{S}}_I, \qquad (3)$$

in which effective magnetic fields are

$$\boldsymbol{h}_{\mathrm{eff},c} = xN_0J_{s-d}\left\langle\hat{\boldsymbol{S}}\right\rangle,$$
$$\boldsymbol{h}_{\mathrm{eff},v} = xN_0J_{p-d}\left\langle\hat{\boldsymbol{S}}\right\rangle,$$
$$\boldsymbol{H}_{\mathrm{eff}} = J_{s-d}\left\langle\hat{P}_c\frac{\hat{\boldsymbol{s}}}{V}\right\rangle + J_{p-d}\left\langle\hat{P}_v\frac{\hat{\boldsymbol{s}}}{V}\right\rangle.$$

$\hat{\boldsymbol{S}}_I$ represents the localized spin operator with the magnitude S, and I is the index of the localized spin. V is the crystal volume. $\hat{\boldsymbol{s}}$ and $\hat{P}_n(n = c, v)$ represent carrier spin and a projection operator restricting the considered states to the states represented by conduction- (c) and valence- (v) band edge functions (Table I), respectively. The forms of $\hat{P}_{c,v}\hat{\boldsymbol{s}}$ are

$$\hat{P}_c\hat{\boldsymbol{s}} = \begin{bmatrix} \hat{\boldsymbol{s}}^{(s)} & O_{cv} \\ O_{cv}^\dagger & O_v \end{bmatrix}, \qquad \hat{P}_v\hat{\boldsymbol{s}} = \begin{bmatrix} O_c & O_{cv} \\ O_{cv}^\dagger & \hat{\boldsymbol{s}}^{(p)} \end{bmatrix},$$

in which O_c, O_v, and O_{cv} are 2×2, 6×6, and 2×6 zero matrices. $\hat{\boldsymbol{s}}^{(s)}$ and $\hat{\boldsymbol{s}}^{(p)}$ are spin operators represented by the band-edge functions (Table I), and the matrix forms are

$$\hat{s}_i^{(s)} = \tfrac{1}{2}\sigma_i, \qquad \hat{s}_i^{(p)} = \tfrac{1}{6}\begin{bmatrix} 2J_i & -6T_i^\dagger \\ -6T_i & -\sigma_i \end{bmatrix}, \qquad i = x, y, z,$$

with the i component of the Pauli matrix σ_i, matrices J_i and T_i (please see Appendix A for J_i and T_i).

J_{s-d} and J_{p-d} are the exchange constants for which we used values of the first-principles calculation [50]. N_0 is the number of the cation site per unit volume and is equal to the inverse of the unit-cell volume $a_0^3/4$ in which a_0 is the lattice constant of the host semiconductor [48]. x is the iron concentration.

The localized spin polarization $\langle\hat{\boldsymbol{S}}\rangle$ is the statistical average value of the localized spin and follows the equation of state,

$$\langle\hat{S}\rangle = \frac{H_{\mathrm{eff}}}{H_{\mathrm{eff}}}SB_S\left(\frac{SH_{\mathrm{eff}}}{k_BT}\right),$$
$$B_S(y) = \frac{2S+1}{2S}\coth\left(\frac{2S+1}{2S}y\right) - \frac{1}{2S}\coth\left(\frac{1}{2S}y\right), \qquad (4)$$

in which S is the magnitude of the localized spin ($S = 5/2$ for Fe^{3+}) and $B_S(y)$ is the Brillouin function with Boltzmann constant k_B and temperature T.

The carrier spin polarization density $\langle\hat{P}_n\boldsymbol{s}/V\rangle$ $(n = c, v)$ is the statistical average value of the carrier spin density and obeys the following equation:

$$\left\langle\hat{P}_n\frac{\hat{\boldsymbol{s}}}{V}\right\rangle = \sum_m\int\frac{d^3k}{(2\pi)^3}\langle u_{m,\boldsymbol{k}}|\hat{P}_n\hat{\boldsymbol{s}}|u_{m,\boldsymbol{k}}\rangle f_{\mathrm{FD}}(E_{m,\boldsymbol{k}}). \qquad (5)$$

$u_{m,\boldsymbol{k}}$ is the periodic part of the Bloch function of the energy-band $E_{m,\boldsymbol{k}}$ with the band index m and wave-vector $\boldsymbol{k}$. f_{FD} is the Fermi-Dirac distribution including chemical potential μ. We take the integral range as a cube with $2\pi/a_0$ length for simplicity [11]. This range is the first Brillouin zone of the conventional cell, which is different from the first Brillouin zone of the zinc-blende structure. However, since the $\boldsymbol{k}\cdot\boldsymbol{p}$ method is valid near the Γ point far from the Brillouin zone boundary, the specific shape of the first Brillouin zone makes no essential difference in results. For the numerical integration in the $\boldsymbol{k}$ space, we employ the following discretization and equation,

$$\left\langle\hat{P}_n\frac{\hat{\boldsymbol{s}}}{V}\right\rangle = \textstyle\sum_m\frac{(\Delta k)^3}{(2\pi)^3}\sum_{\boldsymbol{K}}\langle u_{m,\boldsymbol{K}}|\hat{P}_n\hat{\boldsymbol{s}}|u_{m,\boldsymbol{K}}\rangle f_{\mathrm{FD}}(E_{m,\boldsymbol{K}}),$$

in which each axis has the identical discrete width Δk at each discretized $\boldsymbol{K}$ point.

We obtain the energy-bands $E_{m,\boldsymbol{k}}$ by diagonalizing the carrier Hamiltonian $H_0 + H_{\mathrm{ex,c}}$. The $\langle\hat{\boldsymbol{S}}\rangle$ and $\langle\hat{P}_n\boldsymbol{s}/V\rangle$ $(n = c, v)$ [Eqs. (4) and (5)] form a system of equations through

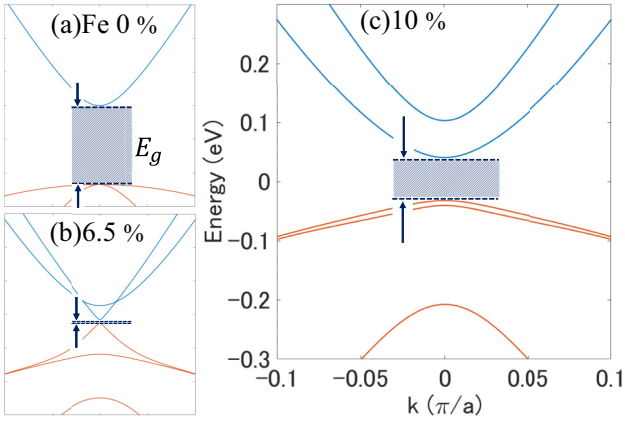

FIG. 2. Energy bands of InFeSb at the iron concentrations of (a) 0, (b) 6.5, and (c) 10%. The horizontal $\boldsymbol{k}$ axis is parallel to the x axis. We also highlight the fundamental energy gap E_g and the development due to the s, p-d exchange interactions by the shaded area. The host semiconductor has the energy gap E_g at the zone center (a). The energy gap becomes closed around the iron concentration of 6.5% (b). The broken gap opens by the s, p-d exchange interactions of the relatively heavy iron doping (c). We plot only the spin-degenerate or spin-split CB, HH, and LH for simplicity.

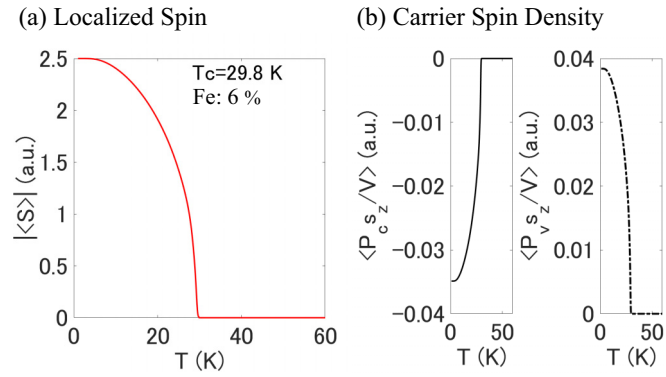

FIG. 3. (a) The temperature dependence of the localized spin polarization $|\langle\hat{S}\rangle|$ at the iron concentration of 6% and electron density of $n_e = 10^{19}$ cm^{-3} for InFeAs. The vertical and horizontal axes represent the magnitude $|\langle\hat{S}\rangle|$ and temperature, respectively. $|\langle\hat{S}\rangle|$ becomes sufficiently small to show the Curie temperature $T_c = 29.8$ K. (b) The temperature dependence of the carrier spin polarization density in conduction- (the left panel) and valence- (the right panel) band-edge representations for the z component [Eq. (5)]. We omit both x and y components since we set $\langle\hat{S}\rangle$ to the z-axis ([001] direction of the host semiconductor).

$H_0 + H_{\mathrm{ex,c}}$, and we have to solve the system of equations self-consistently at each temperature to obtain $\langle\hat{\boldsymbol{S}}\rangle$ and $\langle\hat{P}_n\boldsymbol{s}/V\rangle$. We fix the direction of $\langle\hat{S}\rangle$ to the [001] direction of the host semiconductor for simplicity and confirmed that there was no difference for the magnitude $|\langle\hat{S}\rangle|$ when we changed the direction. The isotropy arises from the Hamiltonian for the localized spins [Eq. (4)]. The Hamiltonian solely contains the effective Zeeman interaction by $\langle\hat{P}_n\boldsymbol{s}/V\rangle$, and not anisotropy terms, for example, single-ion anisotropy. The anisotropy terms reflecting tetragonal symmetry T_d could be incorporated by the crystal field and the relativistic spin-orbit interaction for the localized d orbitals [51].

E. Energy bands and assumptions

Using the multiband $\boldsymbol{k}\cdot\boldsymbol{p}$ Hamiltonian [Eq. (1)], we can explore the electronic structure of n-type FMSs even if the fundamental energy gap E_g [Fig. 2(a)] at the Γ point is broken by s, p-d exchange interactions, and the perturbative effective Hamiltonian [11] is not applicable. We show the energy bands of InFeSb at the iron concentrations of 0, 6.5, and 10% [Figs. 2(a)–2(c), respectively] as a reference. The energy gap at the Γ point decreases with the iron concentration due to the s, p-d exchange interactions and gets closed at the iron concentration of 6.5% [Fig. 2(b)]. After the gap gets broken, the band inversion opens the gap [Fig. 2(c)].

We write the assumptions used in the calculations below for clarity. At first, we neglect the carrier Coulomb interaction [25], which will enhance T_c as the Stoner enhancement. Second, we omit the conduction band at the L point of the first Brillouin zone [48,52], which can appear in relatively high-electron-density systems. Finally, we also neglect the superexchange interaction between iron spins [20,27,53], which is effective in heavy iron-doping FMSs. The neglected effects should be included for quantitative agreement between theory and experiments.

III. FERROMAGNETIC PROPERTIES OF *N*-TYPE FMS

A. InFeAs: Spin polarization and iron concentration dependence of the Curie temperature T_c

Figure 3(a) shows the localized spin polarization $|\langle\hat{S}\rangle|$ at the experimentally typical iron concentration of 6% and electron density of $n_e = 10^{19}$ cm^{-3} [16,24]. We determine the chemical potential μ from the Fermi gas model for the conduction electron that has the effective mass of the host semiconductor CB edge. Starting from the saturation value at a low temperature (1 K), $|\langle\hat{S}\rangle|$ decreases with temperature and vanishes at a certain point. A similar temperature dependence of the magnetization is reported for the p-type GaMnAs in the theory [25] and experiment [26,30]. We approximately extract the Curie temperature T_c at which $|\langle\hat{S}\rangle|$ becomes sufficiently small.

Figure 3(b) depicts the carrier spin polarization density in both conduction- (the left panel) and valence- (the right panel) band-edge representations [Eq. (5)] for the z component. The z component is nonzero below T_c. The x and y components are zero since we fix $\langle\hat{S}\rangle$ to the z axis. When we set $\langle\hat{S}\rangle$ to other directions, we confirmed that the carrier spin density followed the change in direction, and there was no change for T_c and $|\langle\hat{S}\rangle|$.

Figure 4 represents the iron concentration x_{Fe} dependence of T_c. The black symbols are experimental values in measurements [16]. The experiment [16] does not show the exact value of the electron density. However, they estimated the density as the order of 10^{19} cm^{-3} from the donor density and the emergence of ferromagnetism [24]. Therefore, we set the carrier density as 10^{19} cm^{-3}. The red circles are our

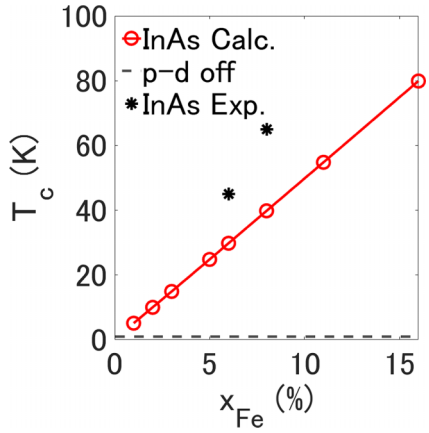

FIG. 4. The iron concentration x_{Fe} dependence of the Curie temperature T_c for InFeAs with the carrier density of 10^{19} cm^{-3}. The black symbols are the experimental values [16]. The red circles represent the calculated T_c of this paper, and we draw the solid line for the guide of the eye. The black dashed line at 1 K represents the *p-d* exchange absent case. On setting the electron density, we discuss in the main text.

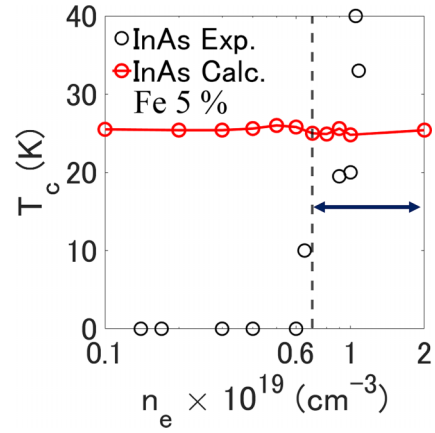

FIG. 5. The electron-density n_e dependence of the Curie temperature T_c for InFeAs at the iron concentration of 5%. The black circles represent the experimental values [24]. The red circles are the calculated T_c of this paper The horizontal arrow and vertical dashed line show the comparable region between the theoretical and the experimental values. Since our theory neglects the localization and other conduction bands, the localization and other conduction-band minima determine the lower and upper bounds, respectively.

calculated values, and we draw the red solid line for the guide of the eye. The calculated T_c linearly depends on x_{Fe}, and this linear dependence is one of the characters for the mean-field approximation [19,20,30]. The black dashed line in Fig. 4 represents the *p-d* exchange absent case, and we confirmed that the T_c is below 1 K.

This drastic decrease is consistent with the estimation in the tunneling spectroscopy [16] in which only the *s-d* exchange interaction of the conduction band was considered. The calculated T_c including the *p-d* exchange fits experimental values well. Therefore, the *p-d* exchange interaction and interband transition, which appear as the *p-d* ESOC [11], are essential for T_c of *n*-type FMSs.

Furthermore, the calculated T_c becomes 127 K at Fe 1% when we neglect remote-band effects ($\gamma_1' = -1$, $\gamma_2' = \gamma_3' = 0$, and $B' = 0$). This T_c value is not realistic since the experimental value of T_c at Fe 6% is 42 K. The remote-band effects are also necessary to explain T_c.

B. InFeAs: Electron density dependence of T_c

Figure 5 shows the calculated T_c for the electron density n_e dependence for InFeAs at the iron concentration of 5%. The T_c of this paper is constant for the electron density, and the ferromagnetism of our $\boldsymbol{k}\cdot\boldsymbol{p}$ model is not a carrier-mediated type. Since the ferromagnetic phase emerges from the *p-d* exchange and interband transition, the T_c does not require the Fermi surface unlike typical carrier-mediated ferromagnets.

The electron-density dependence of T_c was experimentally investigated for InFeAs at the iron concentration of 5% [24], and T_c drastically rises at $n_e = 0.6 \times 10^{19}$ cm^{-3}. This behavior indicates a transition between the Bloch state and the localized state. The transition is typical in doped semiconductors [33], which is known as a localization phenomenon due to Anderson localization [31] and Mott transition [32] by disorder and electron correlation. The localization has been discussed also for the manganese-doped III–V FMSs [28,30].

To analyze T_c through the transition point, we have to account for the interplay among the disorder, electron correlation, and magnetic phase transition. For simplicity, our theory neglects disorder due to the impurity potential and carrier Coulomb interaction for the electronic state since our interest in this paper is in the ferromagnetism by *p-d* ESOC. Therefore, there is a lower bound due to the localization (depicted as the dashed line in Fig. 5), for example, 0.6×10^{19} cm^{-3} in InFeAs (Fe 5%) when we compare the T_c of our $\boldsymbol{k}\cdot\boldsymbol{p}$ model with the experimental values.

An upper bound also exists due to other conduction-band minima. Our theory considers the energy bands located near the Γ point. However, the other conduction-band minima appear in the relatively high-electron density and the second lowest conduction band in InAs is the *L*-point conduction band. The *L*-point conduction-band edge is higher than the Γ point minimum by 0.71 eV [48,52]. The Fermi energy intersects with the *L* point conduction band at the electron density of 2×10^{19} cm^{-3}. In this calculation, we estimate the Fermi energy from the Fermi gas model in which the effective mass is the host semiconductor CB edge value.

The above discussions clarify the comparable region for the comparison of the theoretical T_c with the experimental values, and the region is approximately from 0.7×10^{19} to 2×10^{19} cm^{-3} for InFeAs (Fe 5%). The horizontal arrow and vertical dashed line show the comparable region in Fig. 5. The calculated T_c in the comparable region is on the same order as the experimental values despite using the mean-field approximation and neglecting various effects (for example, disorder and carrier Coulomb interaction). This agreement is sufficient for the investigation of ferromagnetism by *p-d* ESOC. Although the several points in experimental T_c are higher than those of the theoretical one in the comparable region, the calculated value could be enhanced through the carrier Coulomb interaction [25], which is neglected in this paper for simplicity. Our calculation deviates from the ex-

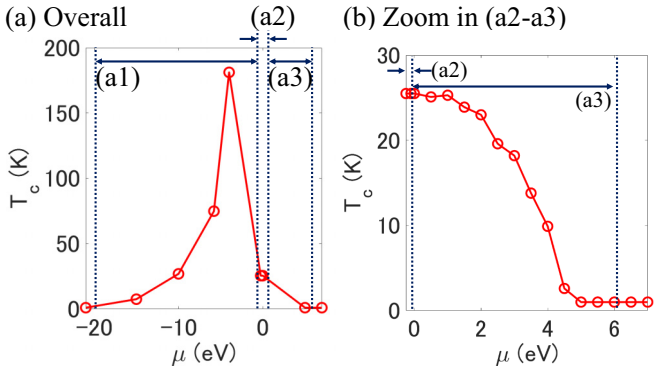

FIG. 6. The chemical potential μ dependence of the Curie temperature T_c. The host semiconductor and iron concentration are the same as the n_e density dependence [Fig. 5]. (a) shows the overall behavior of T_c to separate the region into (a1)–(a3). μ crosses the valence-bands (a1) and conduction-bands (a3) but locates in the bulk band-gap (a2). (b) extracts the (a2) and (a3) region.

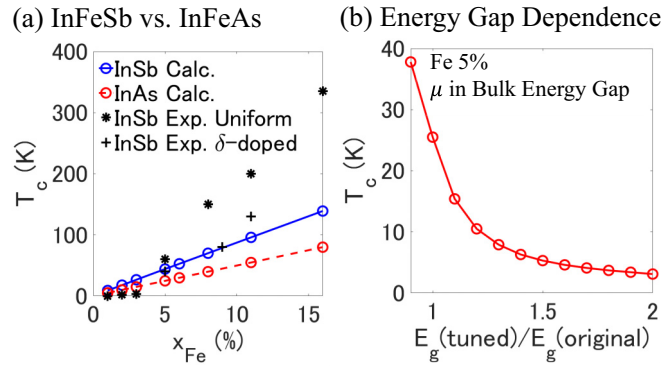

FIG. 7. (a) The iron concentration x_{Fe} dependence of the Curie temperature T_c for InFeSb with the electron density of 1×10^{19} cm^{-3}. The two-type black symbols are the experimental values for uniform iron doping [21] and δ doping [23]. The blue circles are the calculated T_c of this paper, and we draw the solid line for the guide of the eye. We also plot T_c for InFeAs to clarify the host semiconductor dependence by the red circles and dashed line, which is the same as in Fig. 4. (b) T_c dependence on the fundamental energy gap E_g of the host semiconductor for InFeAs (Fe 5%). Since we can theoretically easily fix the number of electrons, we fix the chemical potential μ in the bulk band gap of InFeAs. For the horizontal axis, we take the ratio between the tuned E_g and original E_g.

perimental T_c below the transition point, and we attribute the deviation to the complex localization as discussed above for the lower bound.

We tune the chemical potential μ in Eq. (5) to understand the behavior of our $\boldsymbol{k} \cdot \boldsymbol{p}$ model for T_c. The host semiconductor and iron concentration are identical to the n_e density dependence. We show the μ dependence in Fig. 6 for the overall region [Fig. 6(a)] and the specific zone [Fig. 6(b)].

In Fig. 6(a), we separate the zone into (a1)–(a3) regions. In the region outside (a1) and (a3), all considered bands are empty or occupied, respectively. The T_c vanishes in the outside regions. In (a1), μ crosses the valence bands [HH, LH, and SO in Fig. 1(b)] and T_c gets over 100 K around $\mu = -5$ eV where μ crosses HH and LH resulting in the relatively large density of states. This large T_c is comparable to the Curie temperature of the p-type FMS, such as (III, Mn) As [20], and the considered model is virtually p type. In the (a2) and (a3) regions, μ locates in the bulk band-gap (a2) and crosses the conduction-band (a3).

Figure 6(b) zoom in the (a2) and (a3) region of Fig. 6(a). T_c in the (a2) region is around 25 K whereas μ is included in the bulk band gap. This ferromagnetism emerges from the interband contribution to the spin magnetic susceptibility. The corresponding situation appears in the anomalous quantum Hall system [38] and the interband transition term generates the spin susceptibility in the bulk band insulator. In region (a3), μ starts to cross the conduction bands, and T_c decreases to the fully occupied situation in the conduction bands.

C. InFeSb: Iron concentration and host semiconductor dependence of T_c

We also study the Curie temperature T_c of InFeSb to get insights into the host semiconductor dependence since experiments observed higher T_c in InFeSb than InFeAs [21,23]. Figure 7(a) represents the calculated T_c with the linear dependence on the iron concentration by the blue circles and solid line. These calculated T_c in the lower-concentration region are on the same order as the experimental values [21,23], which are plotted by the black symbols in Fig. 7(a). For quantitative agreement in the higher concentration region, we have to incorporate further exchange interactions between iron ions, for example, superexchange interaction. We confirmed that the calculated T_c became lower than 1 K without the p-d exchange interaction of the valence band, and the p-d exchange plays a dominant role also in the T_c of InFeSb.

Figure 7(a) also contains the calculated T_c of InFeAs, which is the same as in Fig. 4. The calculated T_c values of InFeSb are higher than those of InFeAs, and this host semiconductor dependence is consistent with the experiments [16,21,23,24].

We can attribute the T_c difference between InFeSb and InFeAs mainly to the energy-band structure of the host semiconductor, not to the difference in the magnitude of the exchange interactions. The s-d and p-d exchange interactions of InFeSb are slightly larger than the exchange interactions of InFeAs, and the difference cannot make a large difference for T_c since T_c is proportional to J_{p-d}^2 [19,20,30].

We account for the band parameters of the host semiconductor to get a qualitative understanding of the p-d ESOC effect on T_c. The important factor in the host semiconductor parameters is the fundamental energy-gap E_g at the Γ point since the effective Hamiltonian of the p-d ESOC depends on E_g^{-1} in the lowest order of the perturbation form [11]. The effective Hamiltonian contains also Kane matrix element P representing the interband transition. However, P is just weakly dependent on the semiconductors [47]. For example, the material dependence of P is neglected even for the calculation of the electronic structure in heterostructure systems explicitly containing the material dependence [54]. The difference in P between InAs and InSb is a minor contribution to the semiconductor dependence. Therefore, the energy-gap E_g is one of the fundamental band parameters for T_c, and the narrower gap host semiconductors obtain larger spin polariza-

TABLE II. The band parameters of this paper. The braket $(\cdots)$ denotes the unit of the parameter. The parameters without the braket are dimensionless quantities.

Parameter	In(Fe)As	In(Fe)Sb
E_g (eV)	0.418	0.235
Δ_g (eV)	0.39	0.81
E_P (eV)	21.5	23.3
a_0 (nm)	0.605	0.6479
γ_1	20	34.8
γ_2	8.5	15.5
γ_3	9.2	16.5
B' (eV nm^2)	−0.0329	−0.2999
C_k (eV nm)	−0.0011	−0.00082
A_{s-d} (Fe 3.7%) (eV)	0.02/6	0.03/6
B_{p-d} (Fe 3.7%) (eV)	−0.22/6	−0.25/6
$N_0J_{s-d} = 6A_{s-d}/(xS)$ (eV)	0.2162	0.3243
$N_0J_{p-d} = 6B_{p-d}/(xS)$ (eV)	−2.3784	−2.7027

tion in all energy bands from the *p-d* exchange interaction and interband transition to result in higher Curie temperature.

From the host semiconductor dependence [Fig. 7(a)], E_g turns out to be fundamental in the band parameters of our $\boldsymbol{k}\cdot\boldsymbol{p}$ model. To understand the E_g dependence of T_c, we tuned the E_g in InFeAs (Fe 5%) [Fig. 7(b)]. We fix the chemical potential μ position in the bulk energy gap since we can technically easily fix the number of electrons. Figure 7(b) shows the increasing T_c with decreasing E_g. Therefore, we confirmed that the T_c by the *p-d* exchange and interband process includes E_g as one of the essential factors.

IV. CONCLUSION

We studied the ferromagnetic properties (Curie temperature T_c and spin polarization of carrier and localized spin) by *p-d* ESOC in *n*-type FMSs, using the mean-field and $\boldsymbol{k}\cdot\boldsymbol{p}$ methods.

The self-consistent calculation of T_c reaches the same order as the experimental T_c [16,21,23,24] both in InFeAs and in InFeSb for the low iron concentration and intermediate electron-density regions, and reproduces the host semiconductor dependence. The *p-d* exchange interaction and interband transition (*p-d* ESOC) are essential for the T_c of our model for *n*-type FMSs.

Since *p-d* ESOC is based on the interband transition, the ferromagnetism of our $\boldsymbol{k}\cdot\boldsymbol{p}$ model does not require the Fermi surface. This feature gives rise to T_c independent of the electron density. The comparable region for the electron-density dependence has lower and upper bounds. The lower bound appears due to the localization of the disorder and electron correlation, which are neglected in this paper for simplicity. The upper bound exists since the theory considers the energy bands near the Γ point. The chemical potential μ dependence clarifies the global behavior of the considered $\boldsymbol{k}\cdot\boldsymbol{p}$ model for the ferromagnetism, and the model depending on μ becomes *p*-type FMS, bulk band insulator ferromagnet, and *n*-type FMS in each region of Fig. 6.

We confirm higher T_c in the narrower gap host semiconductor (InFeSb) and qualitatively explain the host semiconductor dependence from the energy gap of the host semiconductor with the effective Hamiltonian of the *p-d* ESOC [11]. The narrower gap host semiconductors enhance the *p-d* ESOC to result in higher T_c. We also confirm the fundamental energy-gap dependence of T_c in Fig. 7(b) quantitatively. Using a narrower gap host semiconductor is an effective way to enhance T_c in *n*-type FMSs.

Further quantitative agreement for each dependence may be achieved by introducing other effects neglected in this paper: other conduction bands in relatively high carrier doping [48,52], fluctuation of conduction electron and localized spin, localization by disorder [31] and electron correlation [32], magnetic anisotropy due to the tetragonal crystal field and relativistic spin-orbit coupling of the localized *d* orbitals [51], carrier-carrier interaction [25], and superexchange interaction between iron ions [20,27,53].

The framework of this paper is the combination of the mean-field and $\boldsymbol{k}\cdot\boldsymbol{p}$ methods with exchange interactions of the multiple energy bands, and the theory is not limited to specific materials. Therefore, this framework is useful for the investigation of both relativistic and exchange spin-orbit coupling to open the possibility of other materials for the fundamental properties and spintronics applications.

ACKNOWLEDGMENTS

We are grateful to H. Akera for fruitful discussions. This work was supported by Grant-in-Aid for Scientific Research (C) Grant No. JP21K03413 from the Japan Society for the Promotion of Science (JSPS) and JSPS KAKENHI Grant No. JP22J10913.

APPENDIX A: MATRICES OF J_i AND T_i

The specific forms for matrices J_i and T_i are as follows [47]:

$$J_x = \frac{1}{2}\begin{bmatrix} 0 & \sqrt{3} & 0 & 0 \\ \sqrt{3} & 0 & 2 & 0 \\ 0 & 2 & 0 & \sqrt{3} \\ 0 & 0 & \sqrt{3} & 0 \end{bmatrix},$$

$$J_y = \frac{i}{2}\begin{bmatrix} 0 & -\sqrt{3} & 0 & 0 \\ \sqrt{3} & 0 & -2 & 0 \\ 0 & 2 & 0 & -\sqrt{3} \\ 0 & 0 & \sqrt{3} & 0 \end{bmatrix},$$

$$J_z = \frac{1}{2}\begin{bmatrix} 3 & 0 & 0 & 0 \\ 0 & 1 & 0 & 0 \\ 0 & 0 & -1 & 0 \\ 0 & 0 & 0 & -3 \end{bmatrix},$$

$$T_x = \frac{1}{3\sqrt{2}}\begin{bmatrix} -\sqrt{3} & 0 & 1 & 0 \\ 0 & -1 & 0 & \sqrt{3} \end{bmatrix},$$

$$T_y = \frac{-i}{3\sqrt{2}}\begin{bmatrix} \sqrt{3} & 0 & 1 & 0 \\ 0 & 1 & 0 & \sqrt{3} \end{bmatrix},$$

$$T_z = \frac{\sqrt{2}}{3}\begin{bmatrix} 0 & 1 & 0 & 0 \\ 0 & 0 & 1 & 0 \end{bmatrix}.$$

APPENDIX B: BAND PARAMETERS

Table II summarizes the band parameters of *n*-type FMSs used in this paper. For the host semiconductor band parameters, we use the recommended values [48] without any changes since the clear modification of crystal structure by iron doping has not been observed experimentally [16–18,24,55–58]. For $B' = (B_{8v}^{+} + B_{7v})/2$ and C_k, we employ the values of the literature [47]. We estimate the effective mass m_c in Eq. (2) from the following equation:

$$\frac{m_0}{m_c} = 1 + \frac{E_P}{3}\left(\frac{2}{E_g} + \frac{1}{E_g + \Delta_g}\right),$$

which reproduces the experimental value of the conduction-band effective mass.

The first-principles calculation [50] gives us spin splitting due to the *s-d* and *p-d* exchange interactions at the iron concentration of $x = 3.7\%$. We use the spin splitting values for the *s*, *p-d* exchange interaction coefficients A_{s-d}, B_{p-d} and transform them to N_0J_{s-d}, N_0J_{p-d} by the equation,

$$N_0J_{s-d} = 6A_{s-d}/(xS), \qquad N_0J_{p-d} = 6B_{p-d}/(xS),$$

in which $S = 5/2$, and N_0J_{s-d}, N_0J_{p-d} are independent of the iron concentration. The signs of the coefficients have remained unknown experimentally and theoretically. We follow the typical signs of the III–V manganese-type FMS [20].

[1] K.-H. Ahn, A. Hariki, K.-W. Lee, and J. Kuneš, Antiferromagnetism in RuO_2 as *d*-wave Pomeranchuk instability, Phys. Rev. B **99**, 184432 (2019).

[2] H. Bai, L. Han, X. Y. Feng, Y. J. Zhou, R. X. Su, Q. Wang, L. Y. Liao, W. X. Zhu, X. Z. Chen, F. Pan, X. L. Fan, and C. Song, Observation of Spin Splitting Torque in a Collinear Antiferromagnet RuO_2, Phys. Rev. Lett. **128**, 197202 (2022).

[3] A. Bose, N. J. Schreiber, R. Jain, D.-F. Shao, H. P. Nair, J. Sun, X. S. Zhang, D. A. Muller, E. Y. Tsymbal, D. G. Schlom *et al.*, Tilted spin current generated by an antiferromagnet, Nat. Electron. **5**, 263 (2022).

[4] R. González-Hernández, L. Šmejkal, K. Výborný, Y. Yahagi, J. Sinova, T. Jungwirth, and J. Železný, Efficient Electrical Spin Splitter Based on Nonrelativistic Collinear Antiferromagnetism, Phys. Rev. Lett. **126**, 127701 (2021).

[5] L. Šmejkal, A. B. Hellenes, R. González-Hernández, J. Sinova, and T. Jungwirth, Giant and Tunneling Magnetoresistance in Unconventional Collinear Antiferromagnets with Nonrelativistic Spin-Momentum Coupling, Phys. Rev. X **12**, 011028 (2022).

[6] L. Šmejkal, J. Sinova, and T. Jungwirth, Emerging Research Landscape of Altermagnetism, Phys. Rev. X **12**, 040501 (2022).

[7] M. Naka, Y. Motome, and H. Seo, Perovskite as a spin current generator, Phys. Rev. B **103**, 125114 (2021).

[8] L.-D. Yuan, Z. Wang, J.-W. Luo, and A. Zunger, Strong influence of nonmagnetic ligands on the momentum-dependent spin splitting in antiferromagnets, Phys. Rev. B **103**, 224410 (2021).

[9] L.-D. Yuan, Z. Wang, J.-W. Luo, E. I. Rashba, and A. Zunger, Giant momentum-dependent spin splitting in centrosymmetric low-*z* antiferromagnets, Phys. Rev. B **102**, 014422 (2020).

[10] S. Hayami, Y. Yanagi, and H. Kusunose, Bottom-up design of spin-split and reshaped electronic band structures in antiferromagnets without spin-orbit coupling: Procedure on the basis of augmented multipoles, Phys. Rev. B **102**, 144441 (2020).

[11] K. Hayashida and H. Akera, Spin splitting of the conduction band by exchange interaction in the valence band through a $k \cdot p$ interband process in ferromagnetic semiconductors, Phys. Rev. B **105**, 235203 (2022).

[12] T. Berlijn, P. C. Snijders, O. Delaire, H.-D. Zhou, T. A. Maier, H.-B. Cao, S.-X. Chi, M. Matsuda, Y. Wang, M. R. Koehler, P. R. C. Kent, and H. H. Weitering, Itinerant Antiferromagnetism in RuO_2, Phys. Rev. Lett. **118**, 077201 (2017).

[13] Z. H. Zhu, J. Strempfer, R. R. Rao, C. A. Occhialini, J. Pelliciari, Y. Choi, T. Kawaguchi, H. You, J. F. Mitchell, Y. Shao-Horn, and R. Comin, Anomalous Antiferromagnetism in Metallic RuO_2 Determined by Resonant X-ray Scattering, Phys. Rev. Lett. **122**, 017202 (2019).

[14] S. W. Lovesey, D. D. Khalyavin, and G. van der Laan, Magnetic properties of RuO_2 and charge-magnetic interference in Bragg diffraction of circularly polarized x-rays, Phys. Rev. B **105**, 014403 (2022).

[15] S. Karube, T. Tanaka, D. Sugawara, N. Kadoguchi, M. Kohda, and J. Nitta, Observation of Spin-Splitter Torque in Collinear Antiferromagnetic RuO_2, Phys. Rev. Lett. **129**, 137201 (2022).

[16] L. D. Anh, P. N. Hai, and M. Tanaka, Observation of spontaneous spin-splitting in the band structure of an n-type zinc-blende ferromagnetic semiconductor, Nat. Commun. **7**, 13810 (2016).

[17] P. Nam Hai, L. Duc Anh, S. Mohan, T. Tamegai, M. Kodzuka, T. Ohkubo, K. Hono, and M. Tanaka, Growth and characterization of n-type electron-induced ferromagnetic semiconductor (In, Fe)As, Appl. Phys. Lett. **101**, 182403 (2012).

[18] M. Kobayashi, L. D. Anh, J. Minár, W. Khan, S. Borek, P. N. Hai, Y. Harada, T. Schmitt, M. Oshima, A. Fujimori, M. Tanaka, and V. N. Strocov, Minority-spin impurity band in n-type (In,Fe)As: A materials perspective for ferromagnetic semiconductors, Phys. Rev. B **103**, 115111 (2021).

[19] T. Dietl, H. Ohno, F. Matsukura, J. Cibert, and D. Ferrand, Zener model description of ferromagnetism in zinc-blende magnetic semiconductors, Science **287**, 1019 (2000).

[20] T. Dietl, H. Ohno, and F. Matsukura, Hole-mediated ferromagnetism in tetrahedrally coordinated semiconductors, Phys. Rev. B **63**, 195205 (2001).

[21] N. T. Tu, P. N. Hai, L. D. Anh, and M. Tanaka, High-temperature ferromagnetism in new n-type Fe-doped ferromagnetic semiconductor (In,Fe)Sb, Appl. Phys. Express **11**, 063005 (2018).

[22] N. T. Tu, P. N. Hai, L. D. Anh, and M. Tanaka, Heavily Fe-doped ferromagnetic semiconductor (In,Fe)Sb with high Curie temperature and large magnetic anisotropy, Appl. Phys. Express **12**, 103004 (2019).

[23] K. Nishijima, N. T. Tu, M. Tanaka, and P. N. Hai, Fe delta-doped (In,Fe)Sb ferromagnetic semiconductor thin films for magnetic-field sensors with ultrahigh Hall sensitivity, J. Cryst. Growth **511**, 127 (2019).

[24] M. Tanaka, Recent progress in ferromagnetic semiconductors and spintronics devices, Jpn. J. Appl. Phys. **60**, 010101 (2021).

[25] T. Jungwirth, W. A. Atkinson, B. H. Lee, and A. H. MacDonald, Interlayer coupling in ferromagnetic semiconductor superlattices, Phys. Rev. B **59**, 9818 (1999).

[26] K. Y. Wang, R. P. Campion, K. W. Edmonds, M. Sawicki, T. Dietl, C. T. Foxon, and B. L. Gallagher, in *Physics of Semiconductors: 27th International Conference on the Physics of Semiconductors - ICPS-27*, AIP Conf. Proc. No. 772, edited by J. Menendez and C. G. Van de Walle (AIP, Melville, NY, 2005), p. 333.

[27] K. Sato, L. Bergqvist, J. Kudrnovský, P. H. Dederichs, O. Eriksson, I. Turek, B. Sanyal, G. Bouzerar, H. Katayama-Yoshida, V. A. Dinh, T. Fukushima, H. Kizaki, and R. Zeller, First-principles theory of dilute magnetic semiconductors, Rev. Mod. Phys. **82**, 1633 (2010).

[28] T. Dietl and H. Ohno, Dilute ferromagnetic semiconductors: Physics and spintronic structures, Rev. Mod. Phys. **86**, 187 (2014).

[29] T. Jungwirth, J. Wunderlich, V. Novák, K. Olejník, B. L. Gallagher, R. P. Campion, K. W. Edmonds, A. W. Rushforth, A. J. Ferguson, and P. Němec, Spin-dependent phenomena and device concepts explored in (Ga,Mn)As, Rev. Mod. Phys. **86**, 855 (2014).

[30] T. Jungwirth, J. Sinova, J. Mašek, J. Kučera, and A. H. MacDonald, Theory of ferromagnetic (III,Mn)V semiconductors, Rev. Mod. Phys. **78**, 809 (2006).

[31] P. W. Anderson, Absence of diffusion in certain random lattices, Phys. Rev. **109**, 1492 (1958).

[32] N. F. Mott, *Metal-Insulator Transitions* (Taylor and Francis, London, UK, 1990).

[33] T. F. Rosenbaum, K. Andres, G. A. Thomas, and R. N. Bhatt, Sharp Metal-Insulator Transition in a Random Solid, Phys. Rev. Lett. **45**, 1723 (1980).

[34] M. Naka, S. Hayami, H. Kusunose, Y. Yanagi, Y. Motome, and H. Seo, Spin current generation in organic antiferromagnets, Nat. Commun. **10**, 4305 (2019).

[35] N. T. Tu, P. N. Hai, L. D. Anh, and M. Tanaka, (Ga,Fe)Sb: A p-type ferromagnetic semiconductor, Appl. Phys. Lett. **105**, 132402 (2014).

[36] T. Takeda, M. Suzuki, L. D. Anh, N. T. Tu, T. Schmitt, S. Yoshida, M. Sakano, K. Ishizaka, Y. Takeda, S.-i. Fujimori, M. Seki, H. Tabata, A. Fujimori, V. N. Strocov, M. Tanaka, and M. Kobayashi, Hybridization between the ligand p band and Fe$-3d$ orbitals in the p-type ferromagnetic semiconductor (Ga,Fe)Sb, Phys. Rev. B **101**, 155142 (2020).

[37] F. D. M. Haldane, Model for a Quantum Hall Effect without Landau Levels: Condensed-Matter Realization of the "Parity Anomaly," Phys. Rev. Lett. **61**, 2015 (1988).

[38] Q.-Z. Wang, X. Liu, H.-J. Zhang, N. Samarth, S.-C. Zhang, and C.-X. Liu, Quantum Anomalous Hall Effect in Magnetically Doped InAs/GaSb Quantum Wells, Phys. Rev. Lett. **113**, 147201 (2014).

[39] L. Riney, J. Bermejo-Ortiz, G. Krizman, S.-K. Bac, J. Wang, M. Zhukovskyi, T. Orlova, L. A. de Vaulchier, Y. Guldner, R. Winkler, J. K. Furdyna, X. Liu, and B. A. Assaf, Fermi level tuning and band alignment in Mn-doped InAs/GaSb, Phys. Rev. B **105**, 125301 (2022).

[40] E. O. Kane, Band structure of indium antimonide, J. Phys. Chem. Solids **1**, 249 (1957).

[41] E. I. Rashba, Properties of semiconductors with an extremum loop. 1. cyclotron and combinational resonance in a magnetic field perpendicular to the plane of the loop, Sov. Phys. Solid State **2**, 1109 (1960).

[42] F. J. Ohkawa and Y. Uemura, Quantized Surface States of a Narrow-Gap Semiconductor, J. Phys. Soc. Jpn. **37**, 1325 (1974).

[43] Y. A. Bychkov and E. I. Rashba, Oscillatory effects and the magnetic susceptibility of carriers in inversion layers, J. Phys. C **17**, 6039 (1984).

[44] R. Lassnig, $k \rightarrow \cdot p \rightarrow$ theory, effective-mass approach, and spin splitting for two-dimensional electrons in GaAs-GaAlAs heterostructures, Phys. Rev. B **31**, 8076 (1985).

[45] G. Dresselhaus, Spin-orbit coupling effects in zinc blende structures, Phys. Rev. **100**, 580 (1955).

[46] A. A. Abrikosov and L. P. Gor'kov, On the Nature of Impurity Ferromagnetism, Sov. Phys. JETP **16**, 1575 (1963).

[47] R. Winkler, *Spin-Orbit Coupling Effects in Two-Dimensional Electron and Hole Systems*, Springer Tracts in Modern Physics Vol. 191 (Springer-Verlag, Berlin, 2003).

[48] I. Vurgaftman, J. R. Meyer, and L. R. Ram-Mohan, Band parameters for III-V compound semiconductors and their alloys, J. Appl. Phys. **89**, 5815 (2001).

[49] J. M. Luttinger, Quantum theory of cyclotron resonance in semiconductors: General theory, Phys. Rev. **102**, 1030 (1956).

[50] S. Sakamoto and A. Fujimori, Chemical trend in the electronic structure of Fe-doped III$-$V semiconductors and possible origin of ferromagnetism: A first-principles study, J. Appl. Phys. **126**, 173910 (2019).

[51] K. Yosida, *Theory of Magnetism*, Springer Series in Solid-State Sciences (Springer, Berlin/Heidelberg, 2010).

[52] J. R. Chelikowsky and M. L. Cohen, Nonlocal pseudopotential calculations for the electronic structure of eleven diamond and zinc-blende semiconductors, Phys. Rev. B **14**, 556 (1976).

[53] P. W. Anderson, New approach to the theory of superexchange interactions, Phys. Rev. **115**, 2 (1959).

[54] G. Bastard, *Wave Mechanics Applied to Semiconductor Heterostructures* (Halsted, Les Ulis, France, 1988).

[55] P. Nam Hai, L. D. Anh, and M. Tanaka, Electron effective mass in n-type electron-induced ferromagnetic semiconductor (In,Fe)As: Evidence of conduction band transport, Appl. Phys. Lett. **101**, 252410 (2012).

[56] L. Duc Anh, P. Nam Hai, and M. Tanaka, Control of ferromagnetism by manipulating the carrier wavefunction in ferromagnetic semiconductor (In, Fe)As quantum wells, Appl. Phys. Lett. **104**, 042404 (2014).

[57] M. Kobayashi, L. D. Anh, P. N. Hai, Y. Takeda, S. Sakamoto, T. Kadono, T. Okane, Y. Saitoh, H. Yamagami, Y. Harada, M. Oshima, M. Tanaka, and A. Fujimori, Spin and orbital magnetic moments of Fe in the n-type ferromagnetic semiconductor (In, Fe)As, Appl. Phys. Lett. **105**, 032403 (2014).

[58] D. Sasaki, L. D. Anh, P. Nam Hai, and M. Tanaka, Interplay between strain, quantum confinement, and ferromagnetism in strained ferromagnetic semiconductor (In, Fe)As thin films, Appl. Phys. Lett. **104**, 142406 (2014).